JGR Solid Earth

RESEARCH ARTICLE
10.1029/2018JB016902

Accurate Depth Determination for Moderate-Magnitude Earthquakes Using Global Teleseismic Data

T. J. Craig[1]

[1]Institute of Geophysics and Tectonics, School of Earth and Environment, University of Leeds, Leeds, UK

Key Points:
- I present a method for stacking global seismic data to extract coherent depth phases
- The observation of multiple depth phases allows for the near-automatic determination of source depths for earthquakes down to M_w 4.9
- As a regional example, I show the results of this technique as applied to 324 earthquakes in the North Chile subduction zone

Supporting Information:
- Supporting Information S1
- Table S1

Correspondence to:
T. J. Craig,
T.J.Craig@leeds.ac.uk

Citation:
Craig T. J. (2019). Accurate depth determination for moderate-magnitude earthquakes using global teleseismic data. *Journal of Geophysical Research: Solid Earth*, *124*. https://doi.org/10.1029/2018JB016902

Received 20 OCT 2018
Accepted 26 JAN 2019
Accepted article online 30 JAN 2019

Abstract The determination of accurate source depths for globally observed earthquakes has long been one of the most problematic issues in earthquake source seismology. The optimal method for constraining the depths of teleseismically observed earthquakes is through the identification of near-source surface reflections—depth phases. However, observing such phases is complicated by the relatively small amplitude of these arrivals compared to the background noise, particularly for earthquakes with $M_w < 5.5$. In this study, I present a methodology for leveraging the recent expansion in global seismic network coverage to enhance the identification of coherent depth phases through an automated stacking routine using a globally distributed array. While depth solutions for each individual depth phase are often nonunique, the identification of potential depths across multiple different phases, where each shows the correct distance-dependent delay, provides a robust way to semiautomatically determine the source depth of an earthquake. I present a range of examples for the processing routine developed, along with an example for its regional application, to the North Chilean subduction zone. The technique presented offers an opportunity to improve depth estimates for earthquakes down to M_w4.9 and, requiring significantly less analyst input than other techniques offering a similar resolution, has the potential to be applied to large earthquake data sets.

Plain Language Summary The determination of accurate depths for globally observed earthquakes is critical for our understanding of the structure and deformation of tectonic plates but has proven to be one of the most intractable problems in earthquake seismology. Here, I present a method aimed at using the recent vast expansion in global seismic data coverage to enhance the detection of a suite of seismic phases that reflect from the Earths surface directly above the earthquake source—these are often referred to as "depth phases." These phases provide the best known constraint on earthquake depths for remotely observed earthquakes, especially in cases where several of these phases can be observed for a given earthquake. However, they are often difficult to detect, due to their low amplitude, and the complexity of the associated waveform. While limitations remain on the magnitude and source depth ranges over which the technique presented here can be applied, this approach enhances the detection of these low-amplitude phases, allowing them to be identified for smaller earthquakes than has routinely been possible in the past. As this approach uses data observed from around the world, it can potentially be applied to large earthquake data sets in remote areas, where near-field data are unavailable.

1. Introduction

The determination of accurate source depths is one of the most critical aspects of earthquake source seismology, with implications for fields including seismic hazard assessment, lithospheric rheology and structure, and nuclear security. However, it has also remained one of the most elusive problems in observational seismology. It is commonly recognized that, for earthquakes lacking near-source data constraints, the most reliable method of determining accurately the depth at which an earthquake has occurred is through the detection of the principal depth phases (*pP*, *sP*, and *sS*) at teleseismic distances. These phases are near-source surface reflections, but otherwise follow approximately the same path as the associated principal phase (*P* and *S*) through the rest of the Earth (Figure 1). The relative time delay between a depth phase and its associated principal phase hence provides a precise constraint on the traveltime between the earthquake source and the overlying surface. Hence, if the velocity structure above the source is reasonably well known, the relative delay times to these depth phases can be used to provide an accurate estimate of the earthquake source

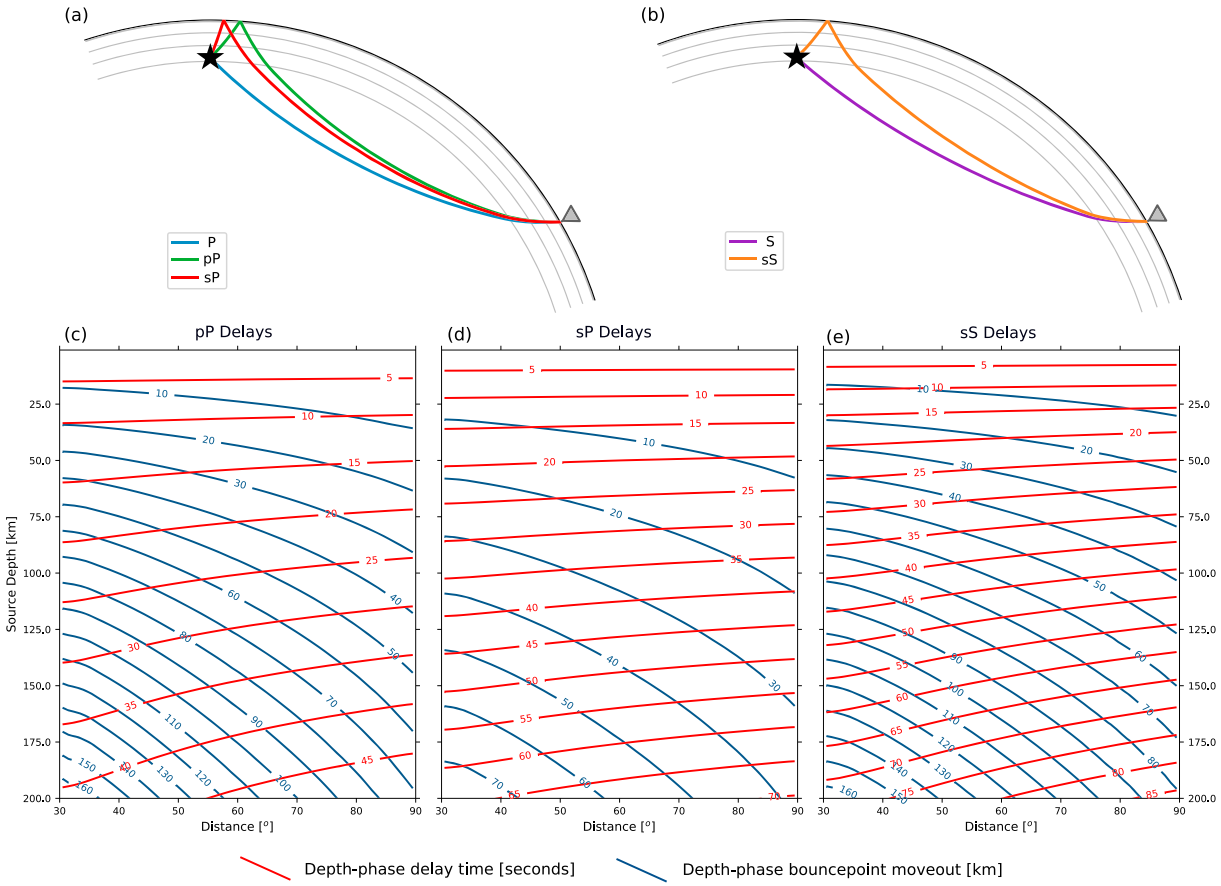

Figure 1. Schematic diagram of propagation paths for the phases *P*, *pP*, and *sP* (a) and for the phases *S* and *sS* (b), observed at a station at teleseismic distances. Depth phase delay times as a function of source depth and epicentral distance for phase pairs (c) *P-pP*, (d) *P-sP*, and (e) *S-sS*, respectively (red contours, in units of seconds). All values are computed for the ak135 Earth Model (Kennett et al., 1995). Blue contours show the moveout of the depth phase bouncepoint from the source epicenter (km).

depth. This depth estimate is independent of the absolute traveltimes of the various phases, and unaffected by any variations in the Earth's velocity structure away from the near-source region.

However, the routine identification of these depth phases, especially for moderate-magnitude ($4.5 < M_w < 6.5$) earthquakes is a complex and difficult process. At shallow depth, the separation time between the onsets of the direct arrival and the subsequent depth phases (see Figure 1) may be less than the duration of the earthquake source itself, leading to the overlap and interference of these phases, and inhibiting onset detection. The depth range over which this takes place is dependent on the source duration, and hence roughly correlates with the earthquake magnitude. Additionally, the detection of depth phases is often complicated by their relatively low amplitude, and the complicated nature of the waveform in the direct phase coda—particularly in areas with a complex near-source velocity structure (see Figure 2).

One of the particular difficulties faced by the detection of depth phases is that the time delay relative to the direct arrival is distance dependent, due to the increase in takeoff angle with distance, and concomitant decrease in the moveout of the near-source bouncepoint from the epicenter (Figure 1). This presents a particular challenge for the commonly applied stacking approaches used to improve the detection of low-amplitude seismic phases (e.g., Florez & Prieto, 2017; Heyburn & Bowers, 2008; Rost & Thomas, 2002), in particular limiting the geographic extent, or aperture, over which data can be stacked before the depth phases cease to be coherent across the array (Murphy & Barker, 2006; Woodgold, 1999). In addition to the problem of the distance-dependent delay of the depth phase arrivals, further complications arise due to the variability in the relative amplitudes and polarities of the direct and depth phase arrivals around the focal sphere, as a function of both azimuth and distance.

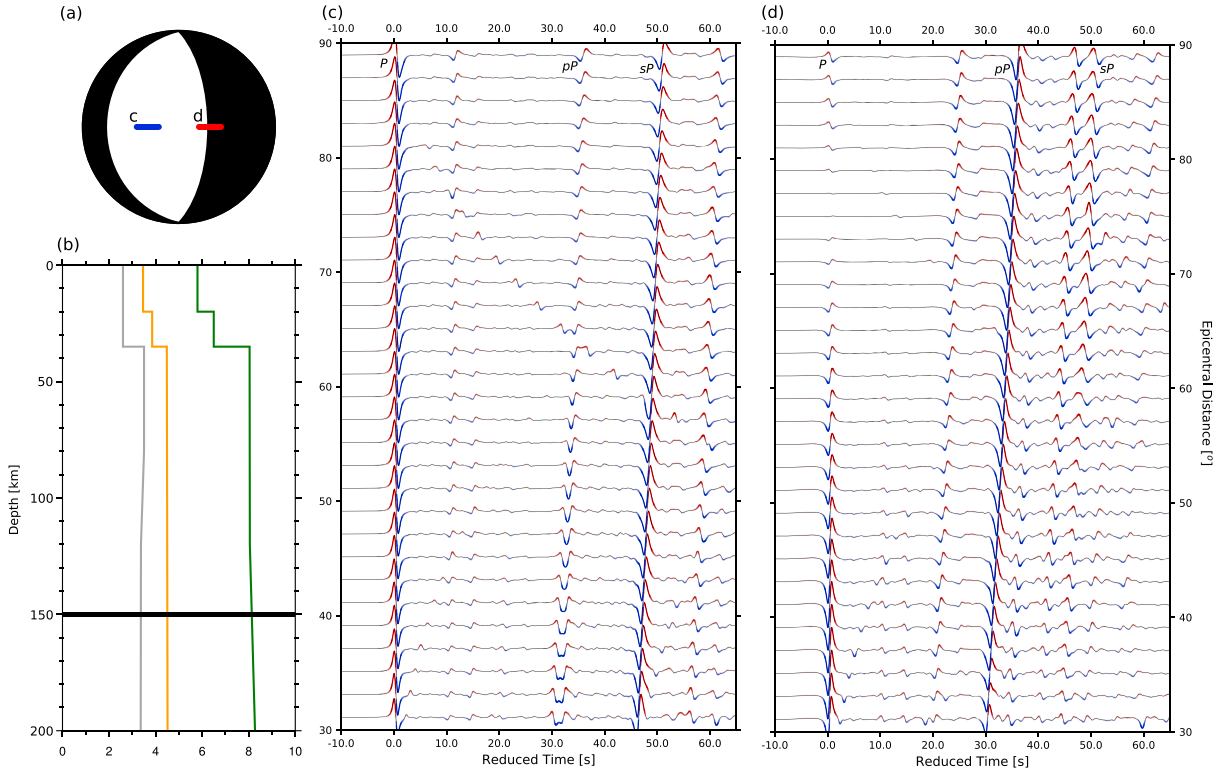

Figure 2. Synthetic waveforms for an earthquake at 150-km depth, computed using the methods of Geller and Ohminato (1994). (a) Earthquake focal mechanism used in calculating synthetic waveforms. Blue and red lines show the pierce points of the synthetic transects shown in (c) and (d), respectively. (b) Velocity structure used in calculating synthetic waveforms. Green line is V_p, gold line is V_s, both in kilometers per second, and the gray line is density in grams per cubic centimeter. The horizontal black line indicates the earthquake source depth. (c) Vertical component waveforms along an azimuth of 90° from the earthquake source, filtered between 0.25 and 2.5 Hz. Annotations indicate the arrivals *P*, *pP*, and *sP*. Amplitudes are normalized by the peak amplitude of each waveform within the window shown. (d) Vertical component waveforms along an azimuth of 270° from the earthquake source.

Figure 2 shows a set of synthetic waveforms for an example intermediate depth earthquake, computed using the Direct Solution method of Geller and Ohminato (1994). These highlight many of the problems faced in identifying depth phases, and using them to constrain the source depth. First, the moveout of the depth phases with increasing epicentral distance can clearly be seen, which prevents simple stacking from resolving the source depth accurately. Second, despite the relatively simple velocity structure used in calculating the waveforms, the *P* wave coda are complex and include a number of other subsidiary phases beyond the principal depth phases. As demonstrated in Figure 2c, these can have significant amplitudes and can often exceed the amplitude of one or other of the main depth phases, further complicating correct phase identification from an individual waveform. Third, the two transects shown in Figures 2c and 2d highlight the problems posed by variable phase polarity. In Figure 2c, the *sP* phase shows a consistent reverse polarity to the direct *P*, where as the *pP*, although smaller in amplitude, flips polarity midway through the distance range shown. In Figure 2d, it is instead the direct *P* and *sP* that change polarity within the distance change shown, while *pP* remains constant. For dip-slip earthquakes with moderate dip angles, polarity changes are not particularly a problem (polarity of both direct and depth phases is consistent across the teleseismic distance range used here), but high-angle dip-slip mechanisms like that used in Figure 2 are particularly sensitive to distance-dependent changes in polarity (and amplitude), while mechanisms with large strike-slip components show greater azimuthal dependence of polarity and amplitude. Simply stacking all global arrivals, even with a distance-dependent window, can hence still lead to incoherent depth phase detection, in cases where data is evenly distributed around the focal sphere.

In this paper, I first briefly summarize existing approaches to earthquake depth determination using depth phases, and then I present an approach to improve the automatic detection of teleseismic depth phases, mitigating many of the problems outlined above, and hence the earthquake source depth. This new approach

is based on the stacking of time-delayed waveform windows, taken relative to the onset of the direct phase arrival, which can be applied to stack all data from a global seismic array.

2. Existing Approaches to Depth Determination

Two main types of approach to the determination of earthquake source depths using teleseismic depth phase data have been developed: those based on the inversion of waveform data, often at longer periods, and those based on the relative delay times of clearly separated depth phases.

2.1. Waveform-Based Methods

2.1.1. Waveform Inversion

The most commonly applied approach to the determination of high-accuracy earthquake depths involves the detailed modeling of a section of the waveform following the direct arrival and including the principal depth phases. This approach, pioneered during the 1970s (e.g., Abe, 1974; Langston, 1976), typically relies upon longer-period data, so as to minimize the influence of near-source velocity structure variations, and to allow the earthquake to be treated as a finite-duration point source or centroid. For the largest earthquakes, above $M_w \approx 6.5$, more complex modeling including multiple sources across a finite-extent fault is required. For earthquakes with long-duration ruptures, or for shallow earthquakes, where the depth phases overlap, a waveform-based approach allows the determination of an accurate source depth without being able to completely separate the depth phases, although such depths remain subject to a series of trade-offs with other mechanism parameters, particularly the rupture duration and moment-rate function. The use of such techniques has been widespread (e.g., Craig et al., 2011, 2014; Devlin et al., 2012; Forsyth, 1982; Huang et al., 1986; Maggi et al., 2000; Solomon & Huang, 1987; Wang et al., 2017; Yang & Chen, 2010), but their application to large-scale data sets has been limited by the requirement for significant analyst input in directing the inversion and in data selection. Further, the sensitivity of higher-frequency components of the waveform to (often poorly constrained) near-source velocity structure variations has limited the development of a stable inversion approach for higher-frequency data, and this has led to such techniques commonly being limited to larger magnitude ($M_w \geq 5.5$) earthquakes, which radiate significant energy at lower frequencies.

2.1.2. Cepstral Methods

A second approach to using the information contained in the waveform relies upon the modulation of the frequency content of the waveform that occurs with each phase arrival. Cepstral methods rely upon taking the Fourier transform of the log frequency spectrum of the waveform, to detect periodicities between arrivals with the same frequency content (Bonner et al., 2002), and hence yields a "cepstrum" with peaks in amplitude associated with separation times between various seismic phases. As the cepstrum returns interphase delays, but not the phases themselves, it remains subject to possible misidentification of delays (e.g., underestimation of depths due to identifying the *pP-sP* delay as *P-pP*) and often struggles in cases with complex *P* wave coda. Such techniques have hence mainly been used in an adjunct capacity to other analytical tools, and, until recently (e.g., Letort et al., 2014, 2015), cepstral techniques have not been widely applied.

2.2. Traveltime-Based Methods

Depth determination using only the traveltimes of direct phase arrivals is subject to significant uncertainty, but the inclusion of the relative delay time to various depth phases leads to a significant reduction in the depth uncertainty (e.g., Bondár et al., 2004; Engdahl et al., 1998, 2006). In addition to the detection and classification of phases directly from observed seismic data, a range of different approaches to the problem of depth phase detection using teleseismic data have been developed over the years, aimed at improving the detection of clearly separated depth phases, and their onset times relative to the direct arrival.

2.2.1. Small-Aperture Arrays

As part of the effort to monitor nuclear testing, a network of small-aperture seismic arrays, often comprising only vertical component short-period instruments, has been developed and is now administered through the International Monitoring System. The dense nature of these arrays, with short interstation distances, and their narrow aperture (typically 10–50 km), make them ideal for the application of relatively simple stacking techniques designed to boost the signal-to-noise ratio of coherent, but relatively small amplitude, signals arriving from a particular direction at the array (Rost & Thomas, 2002). Additionally, these arrays are typically sited in areas chosen for having relatively little near-station variation in seismic velocities and that are remote from common sources of seismic noise, further enhancing the detection of low-amplitude signals.

Beamforming of the waveforms for a small-aperture array hence allows for the detection of depth phases for smaller-magnitude events than is possible using only single-station waveforms and also allows the validation that the signal is arriving at the correct azimuth and slowness (Selby, 2011). Although this network presents a valuable resource, especially for looking at small-magnitude events (e.g., Craig & Heyburn, 2015; Heyburn & Bowers, 2008), the relatively sparse nature of the array network, along with limitations on access to some of the data, prevents its widespread application to global seismicity in an academic context. The lack of multistation three-component data at many of these arrays also hampers the detection of teleseismic *S* waves, leaving depth determination often subject to the ambiguities of *P* wave depth phases and phase misidentification.

2.2.2. Medium-Aperture Arrays

More recently, hybrid approaches using multiple regional-scale arrays and beamforming waveforms on the assumption that the receiver-side velocity structure varies little on a scale of a few hundred kilometers have also been adopted (Florez & Prieto, 2017). This approach then combines depth phase observations from multiple regional arrays across a wider region (e.g., North America) to estimate a robust depth. While this approach mitigates the impact of focal mechanism (due to the small geographic extent of each regional array), the assumption that depth phase moveout is negligible limits the aperture width, and hence the number of stations that can be used. In addition, the approach of Florez and Prieto (2017) assumed that the principal depth phase is always *pP*, which, as shown in Figures 2c and 2d, is not always the case and runs the risk of phase misidentification.

2.2.3. Wide-Aperture Arrays

An alternative approach to the use of smaller-aperture arrays, wherein interstation depth phase delay times can be assumed to be uniform, and simple time shifts allows for stacking of the seismograms, is to use wide-aperture arrays, where stations are grouped over distances of up to 1,000 km. This approach requires that the direct arrival can be identified in each individual trace, and then, assuming a known source-side velocity structure, either applies a time contraction to the following coda prior to stacking (Woodgold, 1999) or stacks distance-variable windows (Murphy & Barker, 2006), to remove the effect of variable delay times at different epicentral distances. This can be done either using the waveform data itself (e.g., Woodgold, 1999), or using binary functions based on possible phase arrivals (e.g., Murphy & Barker, 2006). The resulting stack should then show increased power at the correct delay time for the candidate depth.

Given the vast expansion of global seismic network coverage over the last two decades, these wide-aperture stacking approaches offer the best potential for automatic depth phase-based depth determination, and it is this approach that I develop here for application to a global-scale seismic array.

3. Methodology

The methodology developed here is essentially an extension to that of Woodgold (1999) and Murphy and Barker (2006) to enable the stacking of a global seismic array to enhance the detection of teleseismic depth phases. In summary, this approach involves the identification of the direct arrival on filtered waveform data using a kurtosis-based autopicking routine. The wavelet of the direct phase is then deconvolved from the observed waveform. For each candidate depth, and each candidate depth phase, windows around the predicted delay time relative to the direct arrival are then taken from the correlation trace and stacked to produce a correlation stack as a function of depth for each depth phase. There are then combined to identify depths where there are high coherence signals in the stack for each depth phase.

3.1. Data Selection

I start by taking all broadband seismograms available through FDSN Data Centers at teleseismic distances from the earthquake source, based on the available traveltime-derived catalogue location (typically that from the International Seismological Centre (ISC) or National Earthquake Information Center; see Table S1 in the supporting information). Teleseismic data herein comprises stations between 30° and 90° epicentral distance. Within these limits, body wave arrivals and their coda are clear of the influence of reflected or refracted waves traveling in the structurally complex crust and uppermost mantle and also free from the effects of mantle triplications.

Station responses are removed from each waveform, and three-component records for each station are rotated into vertical and transverse components based on the available catalogue location of the earthquake. Any records with incomplete time series are discarded. Transverse-component waveforms at stations where

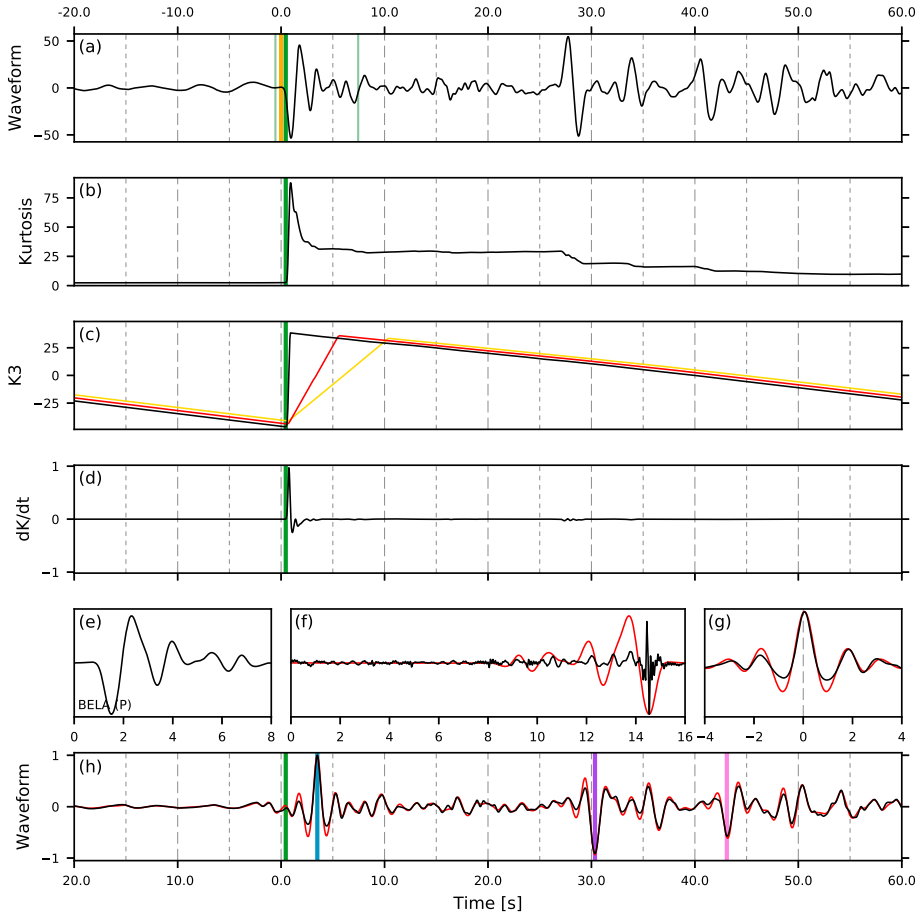

Figure 3. (a) Observed vertical component waveform for a M_w6.3 earthquake on 4 March 2010 beneath northern Chile at 116-km depth, recorded at station BELA (distance 57.9°, azimuth 172.1°), band passed between 0.25 and 2 Hz. Gold line indicated the predicted arrival time based on the catalogue location and origin time. Dark green line is the time of the eventual pick, and light green lines indicate the windown shown in (e), and used for the source deconvolution. (b) Kurtosis. (c) Function K3. Black line is the unaltered K3, colored lines are K3 sequentially smooth with 96- and 48-sample windows. (d) Differential kurtosis. (e) Windowed direct arrival, taken from 1 s before to 7 s after the picked arrival. (f) Deconvolution functions using phase-shift deconvolution (black) or autocorrelation (red). (g) Recovered coherence for the initial source waveform down in (f), when using phase-shift deconvolution (black) or autocorrelation (red). (h) Final correlation trace following deconvolution of the source waveform from the observed trace using either phase-shift deconvolution (black) or autocorrelation (red). Blue line indicated the time of the peak in correlation, shifted from the picked arrival time due to the length of source waveform window used. Purple and pink lines are the predicted arrival times of *pP* and *sP*, respectively, based on the final depth determined, relative the correlation peak for the *P* arrival.

the predicted *S* wave arrival is within 10 s of the predicted arrival of the core phases *SKS* or *PKiKP* are also discarded, to avoid potential misidentification of either of these phases with *S* (misidentification as *sS* is not so much of a problem, as discussed later). Limiting the *S* wave analysis to the use of the transverse component only has the advantage of limiting the observed shear waves to horizontally polarized waves only and hence excludes any complications arising from *P*-to-*S* conversions, such as *pS*. This also excludes any potential water multiples of the upward propagation *p* phase prior to its conversion to a shear wave (ie., *pwS*), reducing the ambiguity in depth phase identification for submarine earthquakes.

All selected waveforms are then subjected to a linear detrend, the removal of a constant value across the trace to produce a zero mean, and are resampled to a uniform sampling rate of 20 samples per second. I then apply a four-pole band-pass filter. The corner frequencies used vary between earthquakes, depending on their magnitude and duration, but default values of 0.25–2.0 Hz for vertical component waveforms, and 0.03–1.0 Hz for transverse component waveforms, were found to produce reasonable results for most earthquakes.

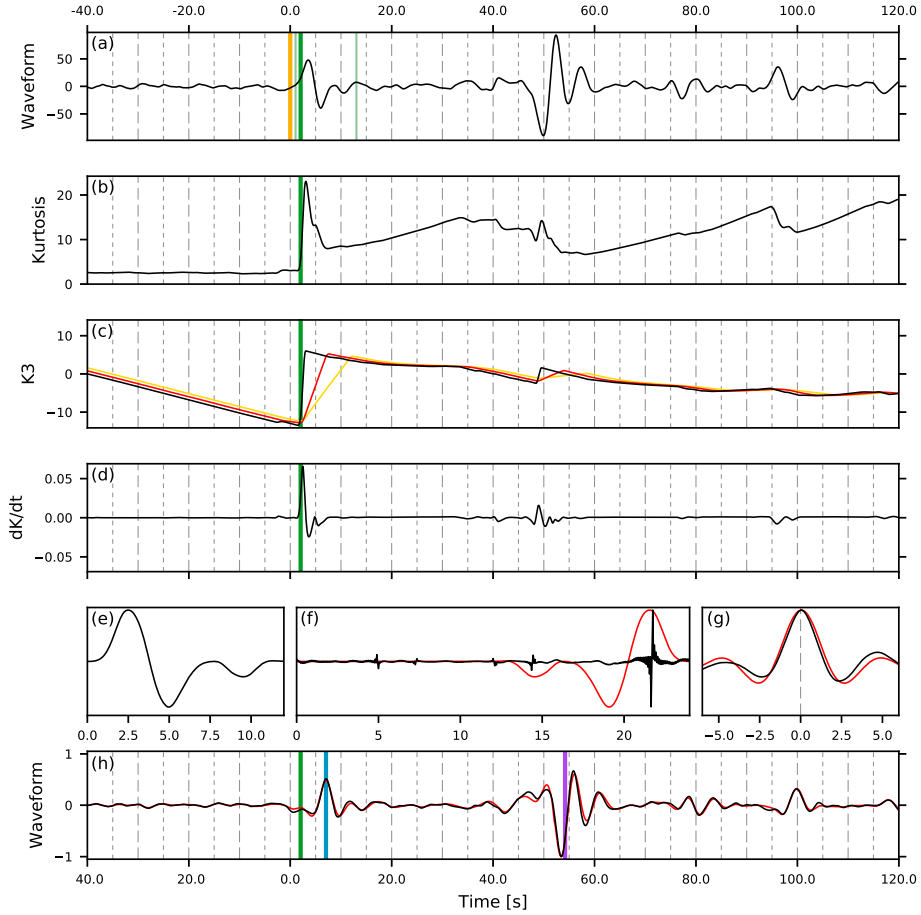

Figure 4. As in Figure 3 but for the transverse component of station 531A (distance 60.9°, azimuth 328.2°), band passed between 0.03 and 1.5 Hz. Source waveform (e) is instead windowed based on 1 s before to 11 s after the direct arrival. Purple line is the predicted *sS* arrival based on the final depth determination, relative to the peak in correlation for the *S* arrival.

3.2. Identification of Direct Arrivals

Initial values for the predicted principal phase arrival are calculated based on the catalog location and depth, using ray tracing through a radially symmetric, one-dimensional Earth model (Kennett et al., 1995). However, to compensate for differences in absolute travel time for different stations, the principal direct phase is required to be detectable in each individual waveform, so that I can stack windows based on predicted depth phase delays relative to this arrival. The following processing steps, aimed at identifying the direct arrival onset, and deconvolving the direct arrival wavelet from the waveform, are exemplified in Figures 3 and 4.

I follow recent approaches in the automated picking of arrivals in microseismic studies (Baillard et al., 2014; Ross & Ben-Zion, 2014; Saragiotis et al., 2002) in using a kurtosis-based approach to automate the process of detecting the direct arrivals.

The kurtosis (K) measures the fourth-order moment of a population, and as such essentially measures the weight of the tails on the population distribution relative to an assumed Gaussian. Mathematically, K is such that

$$K = \frac{\frac{1}{n}\Sigma_{i=1}^{n+1}(x_i - \bar{x})^4}{(\frac{1}{n}\Sigma_{i=1}^{n+1}(x_i - \bar{x})^2)^2} \quad (1)$$

where x is the amplitude of the waveform trace, n is the window length used, and $\bar{x}$ is the mean value of the waveform over the window.

Here, I calculate the kurtosis using window lengths of 60 s (for *P* wave picks) and 30 s (for *S* wave picks). The shorter window used for picking *S* wave arrivals on the transverse component was chosen to minimize the

impact of other coherent phases arriving prior to the direct *S* wave. These window lengths are significantly longer than those used previously in microseismic studies, as a result of the lower-frequency content and longer phase duration of teleseismic body waves.

Phase arrivals based on the peak in the kurtosis trace miss the true onset of the arriving phase, with the peak typically occurring at some later point during the finite duration of the arriving phase. Hence, arrival times are identified using a modified version of the approach of Baillard et al. (2014). The initial kurtosis trace is converted to a function *K*2, such that all negative gradients in the kurtosis trace are removed:

$$K2_{(i+1)} = K2_i + c\frac{\delta K_i}{\delta t} \tag{2}$$

where $c = 1$ if $\frac{\delta K_i}{\delta t} \geq 0$ and $c = 0$ if $\frac{\delta K_i}{\delta t} < 0$, and $K2_{(i=0)} = 0$.

A section of the function *K*2 spanning an 80-s window centered on the predicted arrival time is then subject to a linear detrend (*K*3).

I then calculate two additional sets of *K*3, smoothed over 96 ($K3_{96}$) and 48 ($K3_{48}$) sample windows. Direct phase arrivals are then determined iteratively, first as the principal minimum of $K3_{96}$ within a 15-s window around the predicted arrival time, second as the minimum of $K3_{48}$ within 24 samples of the $K3_{96}$ pick, and finally, as the minimum of the full *K*3 within 12 samples of the $K3_{48}$ pick. This iterative approach mitigates the chance of mispicking the direct arrival due to subsequent phase arrivals producing more significant spikes in the kurtosis than the initial direct arrival, particularly in the case of the *S* wave arrival, which arrives during the *P* wave coda.

Following the determination of direct phase arrival times, I quality control the population of picks, based on both the kurtosis and the differential kurtosis. For a pick to pass, the peak kurtosis value in a 25-sample window starting 5 samples before to 20 samples after the pick time must exceed the average value over a window from 105 samples to 5 samples before the pick time by more than 50%. Additionally, the peak in differential kurtosis must exceed the pre-pick average by a factor of 2.

3.3. Signal Deconvolution

Having identified a subset of waveforms with robust time picks for the direct arrivals, the next step is to window the direct phase wavelet and deconvolve this from the full waveform. This process is particularly advantageous for the extraction of phase arrivals for earthquakes with complex rupture histories and also helps with emphasizing simplistic phase arrivals over the background noise. It also further mitigates the effects of any minor picking errors from the kurtosis-based picking routine outlined above.

The window used in constructing the deconvolution operators used must encompass the full wavelet of the direct phase, along with sufficient padding to allow tapering to zero at the ends. Windows are taken around the identified direct arrival, starting 1 s before the identified arrival time, and with a duration manually selected to encompass the complete direct phase arrival (and therefore the apparent source-time function of the earthquake at each individual station). For the majority of the events considered here, initial trial windows extending to 5 s (for *P* waves) or 7 s (for *S* waves) after the direct phase arrival proved adequate. For larger earthquakes, longer time windows were needed.

Various options exist for deconvolving the windowed principal phase from the waveform trace to identify subsequent arrivals. Here, I follow Woodgold (1999) in applying a phase-shift deconvolution routine. This has the advantage of having a higher temporal resolution than the more commonly used autocorrelation approach and goes some way to reducing the impact of sidelobes in the correlation trace (see Figures 3g and 4g), while remaining stable to minor alteration (and noise) in the original waveform, and does not alter the frequency content of the waveform.

The windowed wavelet is first subjected to cosine tapering of its ends (Figure 3e) and padded with zeros after its end to produce a trace double the time duration of the original window, which starts and ends at zero. The real and imaginary parts of the Fourier transform of this window are then modified to produce the deconvolution operators (Figure 3f). For simple autocorrelation, the transform (T_a) is such that

$$T_a = a - bi \tag{3}$$

and for the phase-shift deconvolution, the transform (T_p) is

$$T_p = \frac{a - bi}{\sqrt{(a^2 + b^2)}} \tag{4}$$

where a and b are the real and imaginary parts of the frequency spectrum from the windowed waveform. The operator is then transformed back into the time domain. In the case of the autocorrelation operator, this is simply the time-reversed waveform.

The final deconvolution operator is then constructed by taking the latter half of this time domain signal, again with cosine taper applied to the first and last 10% of the operator such that the initial and final values are zero. The final correlation trace is then the convolution of this operator with the original waveform (Figure 3h). The arrival time of the direct phase is then modified to account for the timeshift that results from the length of time window used in the deconvolution.

Despite the differences in the operators for the two deconvolution approaches, the resultant correlation trace is similar. However, as shown in Figures 3g and 4g, the phase-shift deconvolution approach systematically improves on the temporal resolution of the signal recovery (albeit marginally) and suppresses the sidelobes resulting from anticorrelation for simplistic wavelets. Hence, I adopt the phase-shift deconvolution approach from this point forward.

3.4. Stacking

Stacks are constructed as a function of depth for each candidate depth phase. For each trial depth, the predicted delay time relative to the direct arrival for each depth phase at each station is used to extract the amplitude of the correlation trace. Amplitudes are extracted in a 12-sample wide window around the nearest sample to the predicted delay time, weighted by a Gaussian function, and then added to the stack. This produces a stack of correlation trace coherence as a function of candidate depth. Delay times for each depth phase are calculated using a ray tracing approach in a one-dimensional spherical Earth (Crotwell et al., 1999). In each case shown here, a locally determined near-source velocity structure is used to modify the shallow structure of the ak135 Earth model (Kennett et al., 1995). Details of the modifications made for use in continental India and northern Chile are given in sections 4 and 5, respectively.

To compensate for the varying degrees of noise present at different stations, each correlation trace is weighted according to the mean amplitude of the noise in a 200 sample (10-s window) taken between 12.5 and 2.5 s prior to the direct phase arrival, before it is added to the stack.

In addition to calculating stacks using the full correlation trace for each phase, stacks are also calculated using the envelope function (Kanasewich, 1981) of the correlation traces. While this loses a significant degree of time resolution, it has the advantage that it is insensitive to the effects of the earthquake focal mechanism on the polarity of the various phases and hence allows all arrivals—no matter where they sit on the focal sphere—to stack coherently.

Stacks are also constructed using a moving window bin through both azimuth and epicentral distance space. These can also help to highlight correct phase arrivals that stack incoherently on the global stack due to polarity variation around the focal sphere. Bin widths of 2.5° for distance and 15° for azimuth are used, with stacks computed at distance intervals of 0.25° for distance and 1° in azimuth. Distance stacks, in particular, are often instructive in correctly identifying *pP* and *sP* arrivals. As both arrivals feature in the *P* wave coda on the vertical component, two separate peaks usually occur in the stacks for each phase—one corresponding to the correct phase, another due to the misidentified alternate phase. The difference in moveout distance between *pP* and *sP* is small enough that both are often reasonably coherent on the global stack. However, as the reduced slowness (slowness relative to the direct arrival) of the two depth phases is different, the misidentified phases show a slanted peak in the distance sweep stack (see Figures 5b and 5e, and 9b and 9e for examples). Similar effects can also often be seen in the *sS* distance sweeps, with markedly different reduced slowness of the *SKS* and *PKiKP* arrivals, which arrive shortly after the direct *S* as the distance approaches 90°, producing a signal that is coherent at shallower candidate depths as distance increases. In all cases, correct phase arrivals should appear as signals that are coherent at all distances at the same depth, without any systematic distance (or azimuth) dependent shift, although phase polarities may change.

The following sections present an example earthquake (the 1997 Jabalpur earthquake) with a well-determined depth from previous studies, as validation of the technique described above, followed by a

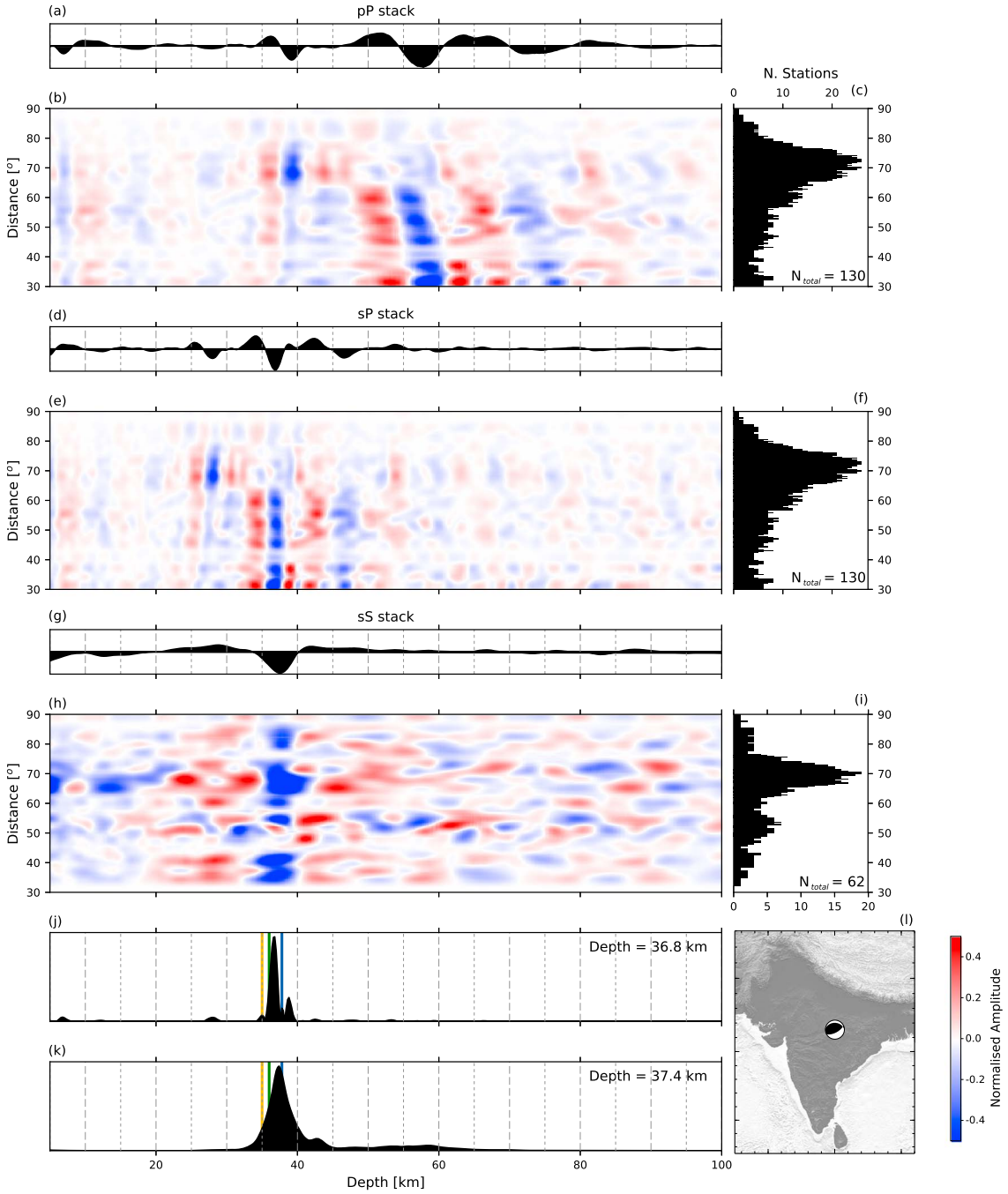

Figure 5. Waveform stacking results for the M_w 5.7 Jabalpur earthquake on 22 May 1997. (a) Global stack for *pP* depth phase delays. (b) Distance sweep for *pP* delays. (c) Distance population used in (b). (d–f) As in (a)–(c) but for *sP* delays. (g–i) As in (a)–(c) but for *sS* delays. (j) Product of the absolute values of (a), (d), and (g). Vertical lines indicate depths from Purnachandra Rao et al. (2002; gold), Singh et al. (1999; green), and Ramesh and Estabrook (1998; blue). Annotation indicates the peak depth value. (k) Product of the stacked envelope functions for each correlation trace. (l) Location map. The amplitudes of all stacks have been normalized for plotting.

regional application to 324 earthquakes from the North Chilean subduction zone, including four processing examples.

4. Validation With Real Data—The 1997 M_W 5.7 Jabalpur, India, Earthquake

The Jabalpur earthquake occurred on 21 May 1997 in central India. It has previously been the subject of a number of seismological studies using a variety of techniques, and as a result has a well established

source depth. Detailed regional and teleseismic waveform inversion indicates a source depth of ~37 km (Purnachandra Rao et al., 2002; Ramesh & Estabrook, 1998; Singh et al., 1999), placing this earthquake within the lower crust of stable India, several kilometers above the local Moho. The majority of the moment release in this earthquake lasted less than 2 s (Ramesh & Estabrook, 1998; Singh et al., 1999), leading to a simple, easily deconvolved, source wavelet, and a significant time separation between all phases, with no phase overlap. In modeling this earthquake, I adopt the crustal velocity structure of Purnachandra Rao et al. (2002), derived using regional *P* and *S* wave travel times, merged into ak135 below the Moho (at 40.2-km depth).

Results for the Jabalpur earthquake are shown in Figure 5. The highest-coherence depth is yielded at depths of 36.8 km for the full stack, and 37.4 km for the enveloped stack, with the stacks for all three candidate depth phases showing peaks in coherence at this depth. This source depth is in good agreement with the previously determined depth estimates from regional waveform modeling (Bhattacharya et al., 1997; Purnachandra Rao et al., 2002; Singh et al., 1999) and is within 1 km of the 37.8-km source depth determined through waveform modeling of teleseismic data (Ramesh & Estabrook, 1998). The ability to automatically and independently match the results of more detailed modeling demonstrates the capacity of the technique described here to determine source depths for moderate-magnitude earthquakes in a near-automatic manner.

Figure 5 highlights a number of important points in interpreting the results from this technique. The presence of two clear peaks in the vertical component highlights the importance of using multiple phases, in order to mitigate phase ambiguity, while the presence of a single clear peak in the *sS* stack emphasizes the importance of including the horizontal component data. The stacks for both *pP* and *sP* show two distinct peaks in coherence, in each case with one peak relating to the correct phase arrival, and a false peak from the alternate depth phase. In this case, due to the orientation of the focal mechanism, *pP* shows an increase in amplitude with distance from the source, and *sP* a decrease in amplitude. Figure 5b in particular clearly shows the negative reduced slowness of the misidentified *sP* phase, leading to a inclined peak in coherence, shallowing with increasing distance. The same phenomenon is visible, although less clearly, in Figure 5e, with the misidentified *pP* showing an increase in coherent depth with distance.

5. Regional Application—The North Chilean Subduction Zone

The North Chilean subduction zone (23.5–18.5°S) offers an ideal test case for the regional application of the techniques developed here. This area is characterized by widespread intermediate depth seismicity associated with the subducting Nazca slab, most notably around the area of the M_w 7.8 2005 Tarapacá earthquake, as well as at shallower depths both within the subducting plate, and along the subduction interface. It has also been the subject of previous studies focused on both the local velocity structure (Husen et al., 1999), and most recently, the compilation of a comprehensive microseismic catalogue, spanning the period from 2007–2014 (Sippl et al., 2018). This presents a scenario where the slab structure and location, along with the regional velocity structure, are relatively well known, and we can test how well a teleseismic catalogue compiled using the approach developed in this study matches the microseismic structure and presents an advance on existing routine approaches.

The techniques developed here are aimed at refining earthquake depths only, and I do not attempt to improve on existing epicentral locations but rather use epicentral locations from the best available traveltime catalogue. Here I use the refined ISC-EHB (EHB; Weston et al., 2018) if available, the EHB (Engdahl et al., 1998) prior to the current completeness of the ISC-EHB, and the National Earthquake Information Center catalogue for more recent earthquakes where neither of these is available (detailed in Table S1). While changes in the depth would result in a change in epicentral location, the resulting shifts are likely to be relatively small (Bondár et al., 2004; Engdahl et al., 1998). Similarly, the effect of using a slightly regionally calibrated one-dimensional velocity model is unlikely to produce major changes in the relative epicentral locations (Engdahl et al., 1998; Engdahl et al., 2006). However, epicentral locations may remain subject to a regional bias due to short-length scale variations in the velocity structure (Engdahl et al., 1998). Consideration of a subset of 722 earthquakes with high-probability codetection in both the local catalogue of Sippl et al. (2018) and the ISC-EHB (Weston et al., 2018) suggests that the average regional shift is ~ 0.18° almost due eastward and is insensitive to the degree of agreement in the depth value in either catalogue. In assessing the improvement offered by the techniques developed in this study, I compare my results to both the best

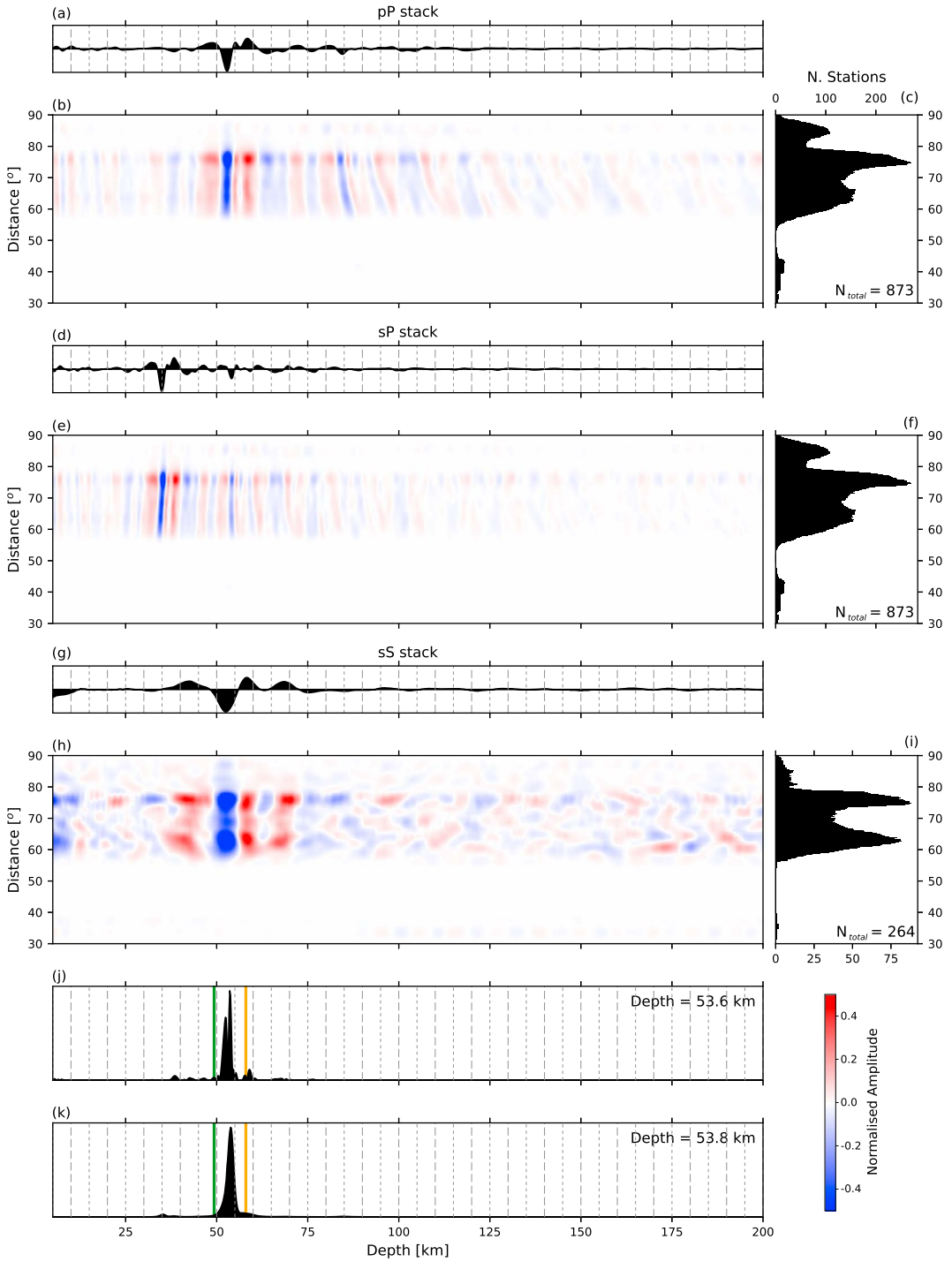

Figure 6. Waveform stacking results for a M_w 5.5 earthquake on 17 July 2010 at −24.7840°N, −69.9650°E. (a) Global stack for *pP* depth phase delays. (b) Distance sweep for *pP* delays. (c) Distance population used in (b). (d–f) As in (a)–(c) but for *sP* delays. (g–i) As in (a)–(c) but for *sS* delays. (j) Product of the absolute values of (a), (d), and (g). Vertical lines indicate the gCMT depth (gold) and the ISC-EHB depth (green). Annotation indicates the peak depth value. (k) Product of the stacked envelope functions for each correlation trace. The amplitudes of all stacks have been normalized for plotting.

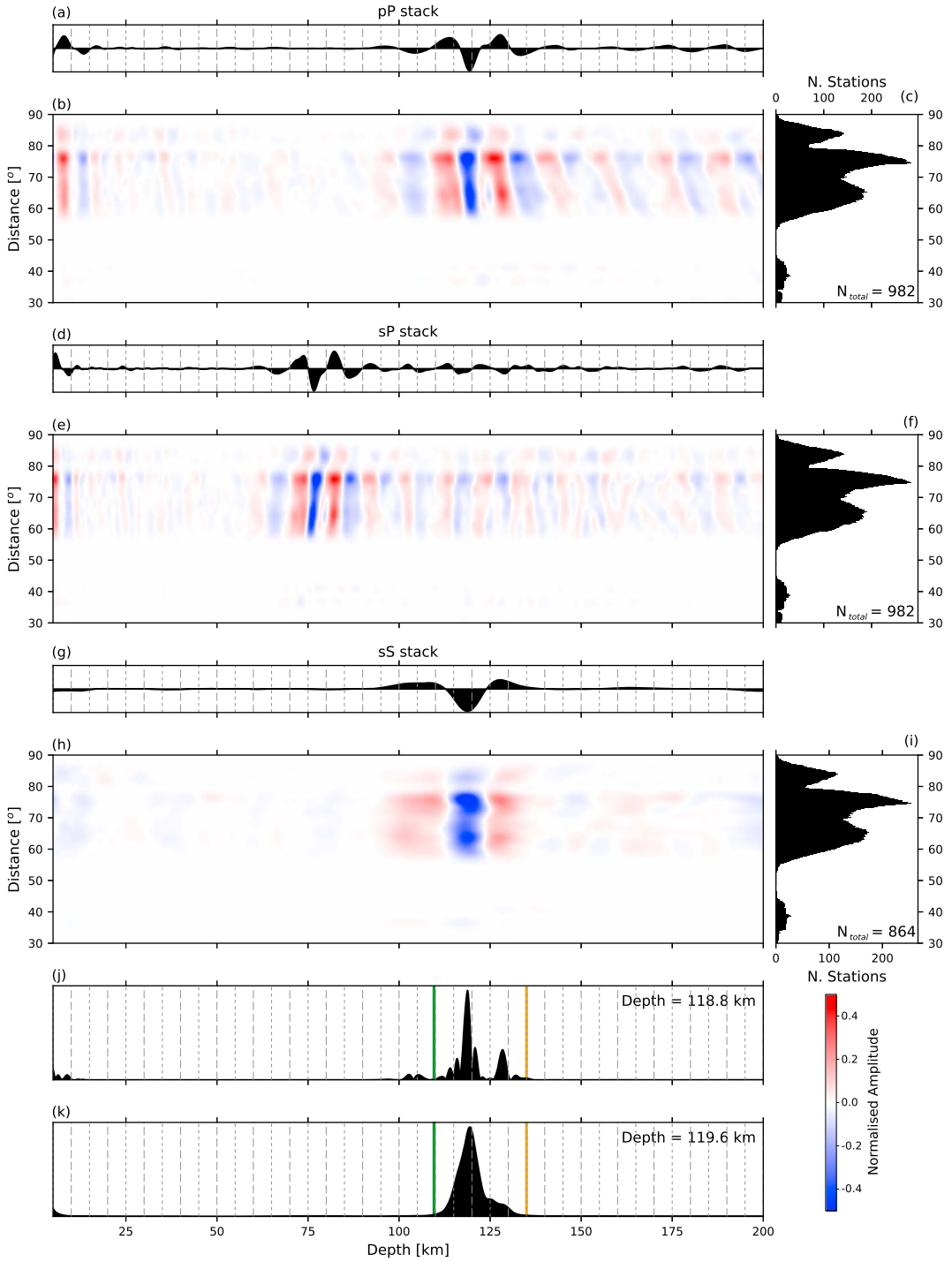

Figure 7. As in Figure 6 but for a M_w 6.2 earthquake on 12 July 2010 at −22.2600°N, −68.3460°E.

available traveltime catalogue locations and depths, and to those derived by the gCMT project (Ekström et al., 2012).

Although there is no theoretical limitation on the use of a two- or three-dimensional near-source velocity structure in the calculation of predicted depth phase delays (provided the velocity structure is well know), the routine developed here is currently limited to a one-dimensional near-source velocity structure. This choice was made for computational ease—it allows the precalculation of all depth phase delay times for all candidate depths within the chosen velocity structure and greatly increases the speed on computation

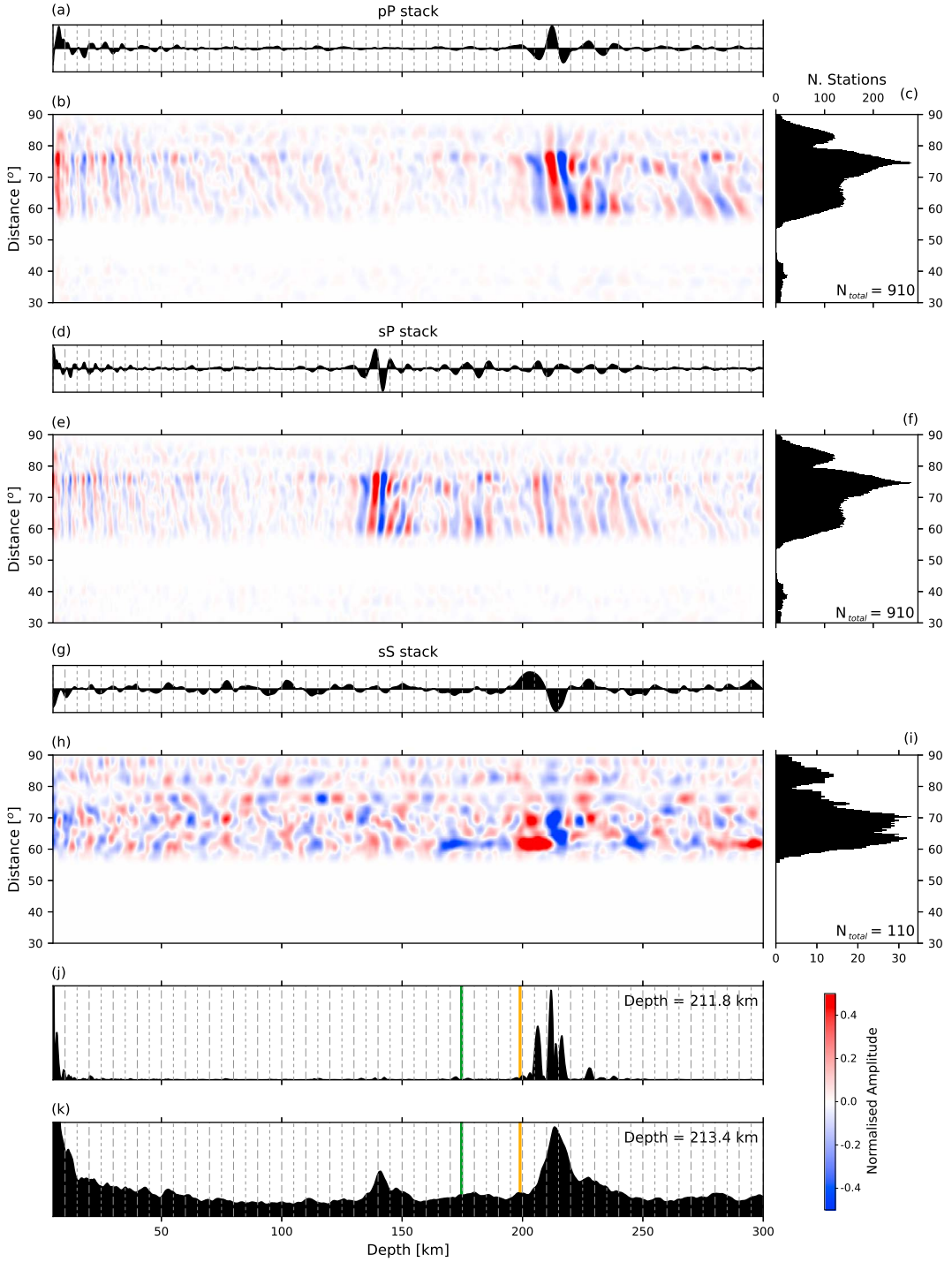

Figure 8. As in Figure 6 but for a M_w 5.2 earthquake on 17 September 2010 at −21.6620°N, −67.1650°E.

for each individual earthquake. It does, however, prevent the use of more complex velocity structure, and removes the potential for accounting for the azimuthal dependence in supra-source velocity common to subduction settings.

To allow comparison between the depths determined here, and the North Chile microseismic locations, the microseismic catalogue used here (from Sippl et al., 2018, and shown in Figures 10 and 11) is one determined within the one-dimensional velocity structure of Husen et al. (1999), rather than the more complex one, based on a two-dimensional velocity structure, used in determining the slab model of Sippl et al. (2018). In

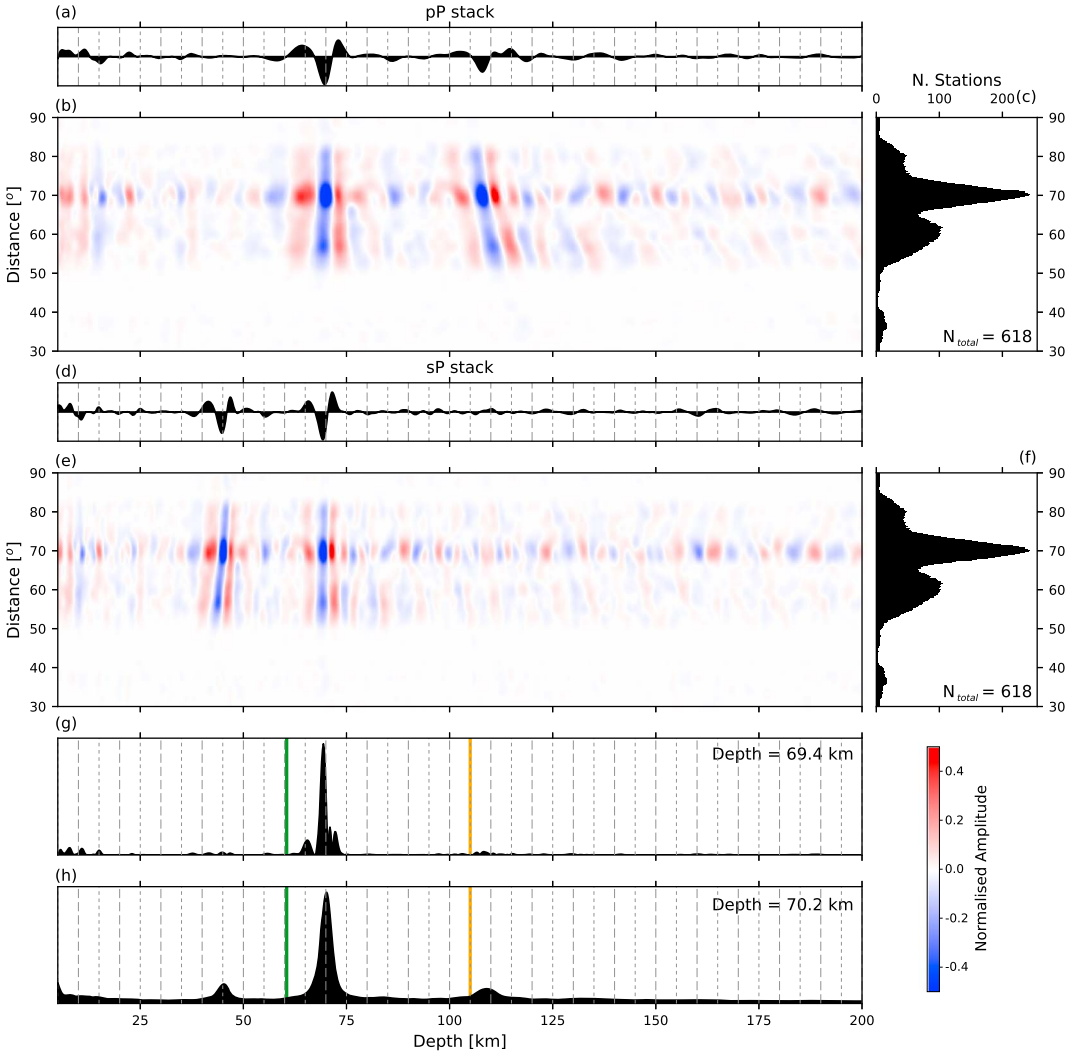

Figure 9. Stacking results for a M_w 5.2 earthquake on 4 September 2017 at −19.2624°N, −70.0039°E, for which no *sS* phase is visible. (a–f) As in Figure 6. (g) The product of the absolute values of (a) and (d). Vertical lines indicate the gCMT depth (gold) and the International Seismological Centre-Engdahl-van der Hilst-Buland depth (green). Annotation indicates the peak depth value. (h) is the product of the stacked envelope functions for *pP* and *sP* delays.

keeping with this, the teleseismic results presented here are computed using the adapted velocity structure of Husen et al. (1999) as employed by Sippl et al. (2018) at depths shallower than 120 km, merging into the global ak135 model below 120 km.

I apply the procedure outlined above to earthquakes reported in the ISC catalogue from 1990–2018 with magnitudes over 4.8 and reported depths over 30 km, in an area from −71.5°E to −66.5°E and −23.5°N to −18.5°N. Three-hundred twenty-four of these earthquakes yielded robust solutions with multiple depth phases detected. Figures 6–9 show a series of examples for the results of applying the technique developed here to intraslab earthquakes from North Chile. The full results are then shown in Figure 10, along with the microseismic catalogue for the same region.

Figure 6 first shows an excellent example for a M_w 5.5 earthquake occurring within the subducting Nazca slab beneath northern Chile. This earthquake shows clear, coherent arrivals with the correct reduced slowness for all three depth phases at a source depth of 53.6 km. The narrow width of the correlation peaks for each phase, and the good alignment between phases, leads to an extremely well constrained depth for this earthquake. This example also serves to illustrate the wealth of data that can be combined for a single earthquake by using the modern global seismic network. For this earthquake from mid-2010, the stacks shown

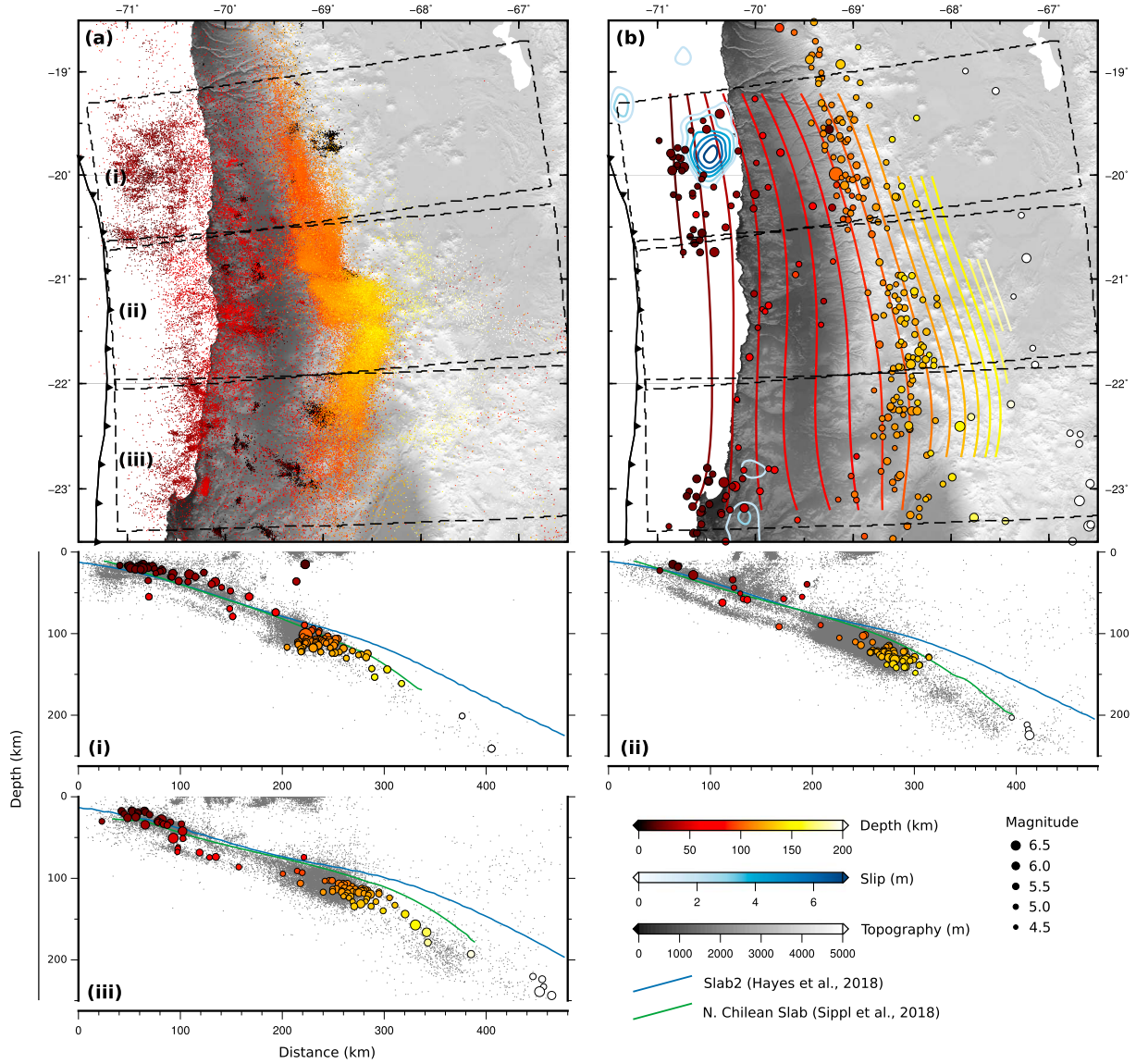

Figure 10. (a) The North Chilean subduction zone. Microseismicity shown is from the catalogue of Sippl et al. (2018), colored by depth. Dashed outlines indicate the extents of the cross sections shown in (i)–(iii). (b) Earthquakes with teleseismically determined depths from this study. Slip contours (blue) show the rupture extents of the 1995, 2007, and both 2014 (all $M_w \geq 7.5$) earthquakes (Hayes, 2017). Contours shaded by depth are the slab-surface model of Sippl et al. (2018). (i)–(iii) Cross sections show seismicity reprojected for each profile as shown in (a). Gray dots are microseismicity from Sippl et al. (2018). Colored points are earthquakes from this study. Lines show the mean depth to the slab top for each distance for Slab2 (Hayes et al., 2018; blue) and from Sippl et al. (2018, green).

in Figure 6 use 893 of the 1,025 available seismograms at teleseismic distances for the vertical component, and 264 of 919 available seismograms for the transverse component, the others being discarded due to either data quality, or as part of the quality control procedure described in section 3.2.

The second example, Figure 7, shows the results from a larger earthquake (M_w 6.2) with a more complex source process to be removed during the deconvolution step. Due to the increased moment and duration of the source, the results for this earthquake lack the fine-scale depth resolution of the earthquake shown in Figure 6 but still yields a well-constrained source depth of 119 km, with a fairly narrow coherent peak. In this example, the source mechanism results in only one of the *P* wave depth phases having a significant amplitude, leading to an ambiguous depth determination if only using vertical component data. However, the presence of a clear *sS* phase allows a robust depth to be determined and confirms that the phase detected in the vertical component is *pP*.

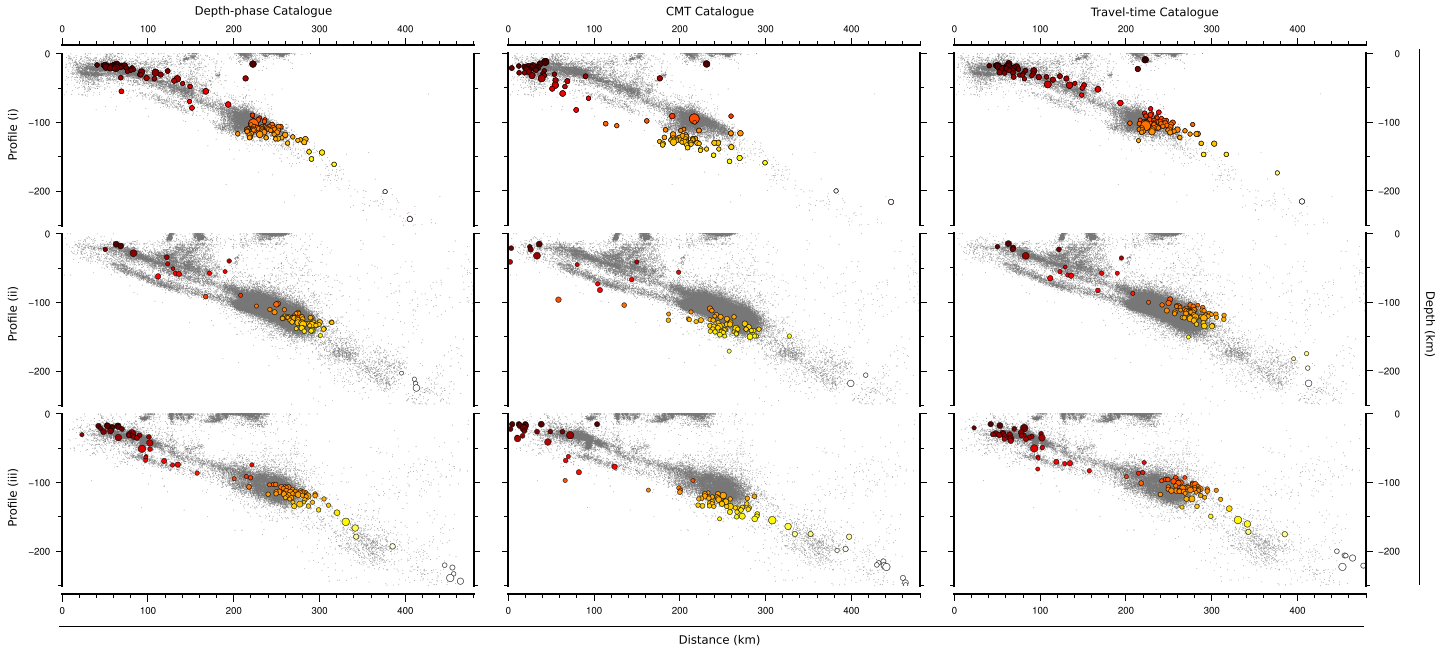

Figure 11. Comparisons between seismogenic slabs as determined from this study (first column), from the gCMT catalogue (second column), and using the best available traveltime-based locations (third column). Profiles are as shown in Figure 10a. Gray dots are microseismicity from Sippl et al. (2018). Scaling and coloring of earthquakes is as in Figure 10.

In the third example, Figure 8, I show the results for a M_w 5.2 earthquake at the deeper end of the depth range applicable for northern Chile—212 km. As Figure 1 demonstrates, for deeper earthquakes, the depth phases experience a much wider spread of bouncepoints, and hence are subject to greater variation in source-side velocity structures. Despite this, and despite the relatively small magnitude of this earthquake, all three depth phases remain coherent for this earthquake. The *pP* stack shows some variability in reduced slowness indicating that the velocity structure used is no longer entirely accurate for earthquakes at this depth (which is entirely expected, given the one-dimensional velocity structure used for the entire region, optimized for a slab top at ~120 km). The *sS* phase is also starting to lose coherence, likely as a result of both the magnitude, frequency content, and depth, of this earthquake. However, despite these issues, a robust depth can still be determined.

Figure 9 shows an example for a M_w 5.2 earthquake where no *sS* phase could be detected from the stacking of horizontal component data, yet a robust depth results from only considering the vertical component data. Both the *pP* and *sP* phases can be clearly identified, with candidate phases with the correct reduced slowness coinciding for a depth of 70 km. As the lower-frequency amplitudes of the *S* wave decreases before that of the higher-frequency *P* wave as source magnitude and duration decrease, the lack of an *sS* arrival is increasingly a problem for smaller earthquakes. The lack of a clear *sS* phase increases the potential for misidentification of the correct *P* wave depth phases, and so only earthquakes where both principal *P* wave depth phases can be seen, coincide at the same candidate depth, and show appropriate reduced slownesses are included. Table S1 indicates the 86 earthquakes, mostly of $M_w \leq 5.2$, where the depth has been determined using only *P* wave depth phases.

Figure 10 shows the results for this regional study of 324 earthquakes under northern Chile. In Figure 10, the locally derived microseismic catalogue is assumed to accurately delineate the subducting Nazca slab beneath the western Andes. Depths determined using the techniques derived here image a seismogenic slab that matches closely with that seen in the microseismic catalogue. No clear separation into discrete double seismic zones in the deeper slab seen in the teleseismic catalogue. However, while there are too few earthquakes large enough to yield teleseismic depths in the shallow portion (< 100 km) of the slab to allow the independent detection of double seismic zones, those teleseismic depths that can be determined correspond nicely with the two planes of seismicity that can be seen in the microseismic catalogue.

It is interesting to note that the depth range of the teleseismically constrained earthquakes is somewhat narrower than the width of the seismogenic slab imaged by the microseismic catalogue (Figure 10, ii and iii) while remaining centered on the same seismogenic slab. This may either be an indication of the variable levels of certainty present in the large microseismic catalogue, leading to a degree of "smearing" in the detected seismogenic slab by less well-constrained earthquakes, or perhaps reflects the effect that the larger rupture extent of the earthquakes large enough to be studied using teleseismic data and indicates that they do not nucleate at the edges of the seismogenic zone.

For comparison to the depth estimates from routine seismic catalogues, I show a series of transects in Figure 11. In terms of depth alone, there is a systematic shift between the two main types of catalogue shown here: the gCMT catalogue routinely estimates increased depths relative to the depth phase constrained depth, while the best available traveltime catalogues (defined above) return an underestimate of the depth. Such a systematic difference cannot be interpreted directly to reflect an incorrect depth, as wholesale shifts in depth may also be the result of the different velocity structures used in the different method proposed (see Figures S1–S3 for examples of this). The depth phase constrained catalogue also eliminates outliers, with both other catalogues considered having a small number of earthquakes with depths outside of the seismogenic zone defined by the subducting slab, and at depths too great to be associated with the overriding plate, which relocated into the confines of the seismogenic slab, using this technique. Finally, despite the limitations of this technique when applied to earthquakes at shallow depths, it appears to do a good job at delineating the plate interface at depths of 20–35 km, with much tighter clustering of seismicity than seen in either of the global catalogues considered.

Figure 10 also shows two available slab models for northern Chile: the Slab2 model of Hayes et al. (2018) and that defined using the local seismic catalogue of Sippl et al. (2018). The Slab2 model features a slab top that is consistently too deep at depths where the interface is seismogenic, and $\sim$ 20 km too shallow once the slab top reaches depths of 100–120 km. In comparison, the locally defined slab model (which is based on a seismicity catalogue using a 2-D velocity structure, rather than that plotted in gray on Figures 10 and 11) matches the relocated seismicity much better, although some discrepancy at shallow depths highlights the unresolved effects of using an oversimplified velocity structure.

6. Error Assessment

The formal quantification of the errors in the depths estimated using this technique is complicated by a number of issues. As a general guide, the width of the peaks present in the various stacks (as illustrated on Figures 5–9) gives a good indication of how well the depth has been constrained. As Figure 7 demonstrates, in cases where the wavelet duration (ie., the rupture duration of the source) is longer, this typically results in a signal dominated by lower frequencies, and, even after deconvolution of the source wavelet, produces a broader peak in the resultant stacks, and lower spatial resolution in depth. However, this does not only reflect an increase in error but also reflects the greater duration (and hence probable spatial extent) of the earthquake source.

The near-source velocity structure used in calculating potential phase delay times represents perhaps the most significant source of uncertainty associated with the technique. In particular, the approach I describe here is highly dependent on knowing reasonably well the V_p/V_s ratio above the source. If this ratio is too far from the true value, then even when coherent phases emerge on each individual phase stack, they fail to align between the various phases, leading to an indeterminate final depth. That the depth estimation results from the combination of two to three different phase observations further complicates the estimation of the uncertainty. In cases where the phases are only slightly out of alignment, as the V_p/V_s ratio is reasonably accurate, misalignment can produce an artificially narrow peak in the final stack of the combined phases, which would, if errors are only based on the width of this peak, lead to an underestimation of the actual error.

Even when the V_p/V_s ratio is correct, errors in the absolute velocity values will produce a systematic shift in the catalogue computed using this technique. In many areas, previous local and regional studies can provide detailed information about the near-source velocity structure (as used in the examples presented here), but this is not always the case, and particularly in the case of remote subduction systems, where little information exists to supplement global models, systematic biases may remain in any data set determined using this approach. In supporting information Figures S1–S3, I show a series of comparisons for the

earthquakes shown in Figures 6–8, calculated with two different velocity structures (the modified one used here for northern Chile, and the global ak135 model). These three earthquakes illustrate well the systematic difference that assumptions about the velocity structure make, with the difference increasing with depth—in this case, from ~ 1 km at 50-km depth, to ~ 10 km at 210-km depth.

As a general guideline, in cases where the various depth phases align well (e.g., Figure 6), errors may be as low a 1 km, compounded by the regionally variable error arising from the velocity structure, which likely increases with increasing depth. However, this represents the best case scenario.

7. Limitations of the Technique

7.1. Velocity Structure

The influence of variations in the surface topography and bathymetry within the radius of the depth phase bouncepoints can play a significant role in altering the relative arrival times, particularly as a function of the receiver azimuth. As Figure 1 demonstrates, for an earthquake depth of 150 km, the relative bouncepoints for two stations at 30° epicentral distance, but on opposite sides of the earthquake, may be up to 300 km apart. In the case of a subduction setting, as discussed in section 5, this would be the difference between bouncepoints under the fore-arc mountain range, and near the subduction trench, with potentially quite different velocity structures. While this is an extreme case, and the station coverage is usually concentrated at greater distance ranges (and hence closer bouncepoints), it serves to illustrate the potential impact that velocity structure can have when combining numerous stations across a wide array aperture.

Without knowing the full three-dimensional velocity structure, and incorporating this into the calculations of relative delays times, there is no way around this problem. However, as demonstrated by the examples shown, particularly Figure 8, this appears not to be a significant issue in depth determination, particularly in cases where the majority of stations are located at large distances from the source, for which the depth phase bouncepoints are more closely clustered near the earthquake epicenter.

Lastly, the presence of a water layer overlying the earthquake source, and the resultant water multiples present in the *P* wave coda may pose problems for oceanic earthquakes, or those associated with oceanic-oceanic subduction. However, as these reverberations reflect multiples of the *pP* depth phase, they can also be used, in an extension to the technique advocated here, and in cases where the water depth is well known (or can be independently determined), to further stack waveform windows, enhancing *pP* detection (Huang et al., 2015). As no water reverberations occur on the transverse component for the *S* wave, limiting earthquake depth determination for subsea earthquakes to those where a coherent *sS* arrival can be seen would also lead to no loss in confidence in depth determination.

7.2. Azimuthal Variability

As illustrated in Figure 2, for earthquakes with steeply dipping nodal planes, the correlation polarity of the depth phases may change as a function of distance. Similarly, the variation in radiation pattern with azimuth (again for earthquakes with steeply dipping nodal planes in either for *P* or *S* wave radiation patterns) can also lead to changes in the correlation polarity of a given phase. In such cases, simply stacking all available waveforms would produce an incoherent stack for the phase in question. This effect is largely countered by doing parameter sweeps through distance (as shown in Figures 5–9) and azimuth space.

The uneven distribution of seismic stations around the world, which are heavily dominated by continental regions, and by particular geographic areas (such as the continental United States, or western Europe), incidentally serves to mitigate this effect, as the azimuthal subarrays for these areas are likely to be coherent, and will dominate the global stack. In the case of northern Chile, for example, North America dominates the data coverage, and while this provides a broad coverage in epicentral distance, it leads to a relatively narrow azimuthal coverage.

7.3. Shallow-Depth Earthquakes

As noted above, for earthquakes occurring at shallow depths, the delay time between the direct and depth phases may be less than the duration of the earthquake source. When this is the case, the approach taken here fails to yield a robust or accurate depth. Few of the earthquakes tried for northern Chile with catalogue depths of ≤ 35-km depth resulted in a robust result. As the duration of an earthquake roughly scales with its magnitude, this lower limit on the depth at which this technique can be applied is magnitude dependent, with smaller earthquakes being workable to shallower depths. Figure 1 summarizes depth phase delay times.

The most critical value in determining potential applicability to shallow earthquakes rests on the separation time between the arrival of *pP* and *sP* (Figure 1)—where the source duration exceeds this time, the two phases cannot be separated, and the depth becomes ambiguous. Hence, for a depth of 25 km to be resolvable, the earthquake source duration should not exceed ~3 s.

7.4. Magnitude Limitations

The processing routine outlines here relies upon the high-confidence identification of the direct arrivals on numerous stations. Empirical testing demonstrates that the autopicking approach taken here typically fails to produce sufficient numbers of high-quality picks once the earthquake magnitude drops below $M_w \sim 4.9$. Additionally, as the earthquake magnitude decreases, and the dominant frequency content goes up, increased attenuation of higher-frequency depth phases leads to severely decreased amplitudes in depth phases, such that even when there are sufficient direct arrivals to attempt a stack, no robust depth can be determined.

7.5. Source Complexity and Duration

More complex source-time functions, and hence more distinct waveforms, result in better phase detection during the deconvolution stage of the processing. However, as noted, longer phase durations cause problems with the overlap of direct and depth phases for shallow earthquakes.

Additionally, the deconvolution stage of the processing assumes that the earthquake source can be treated as a point source and that there is no detectable directivity in the rupture. In cases where this is not valid, the wavelet shape for the different phases would be different, and deconvolution of the direct phase wavelet would not accurately recover the arrivals of phases leaving the earthquake source at different inclinations. While not a major issue for the smaller earthquakes studied here, this limits the accuracy of the technique developed here when applied to larger earthquakes ($M_w \geq 6.5$), where the distributed rupture over a finite-width fault plane becomes apparent.

8. Potential Applications

8.1. Subduction Zones

The principal application of the technique I present here is anticipated to be in refining depth estimates for seismicity associated with the internal deformation of subducting slabs in the upper mantle, in the depth range from 30–300 km, along the lines of the regional example presented in Figure 10. Critical to this will be the expansion of the travel time calculations to incorporate a two-dimensional velocity structure more appropriate to a subduction setting, but even the one-dimensional velocity structure used here represents an advance on currently available techniques. The semiautomated nature of this approach makes it suitable for the large-scale application to all earthquake at M_w 4.9 and above.

8.2. Continental Earthquakes

The limitations with regards to shallow earthquakes (discussed above) will hinder the application of the techniques developed here to continental settings, where the vast majority of earthquakes occur at depths of < 20 km. However, as demonstrated through the Jabalpur earthquake (Figure 5), for regions such as India, East Africa, Tibet, or the forelands of major mountain ranges in South America or Central Asia, where earthquakes occur in the lower crust or uppermost continental mantle (Craig et al., 2011, 2012; Devlin et al., 2012; Sloan et al., 2011), this approach can provide a relatively automatic way to assess earthquake depths.

9. Conclusions

The technique demonstrated here provides a semiautomatic methodology for determining depth phase constrained depths for earthquakes down to M_w 4.9 where large volumes of teleseismic data are available. By stacking distance-dependent windows taken relative to the direct arrival, coherent arrivals corresponding to at least two of the three principal depth phases can be determined for the majority of earthquakes trialed. Analyst input is required in refining appropriate frequency bands and wavelet window lengths to use, and in inspecting results to check for robustness. In a test regional study for the North Chilean subduction zone, depths derived from this technique produce a map of slab seismicity that closely mirrors that previously determined using a high-accuracy local seismic network and represents an improvement on routine global seismic catalogues.

Acknowledgments
This work was supported by a Research Fellowship from the Royal Commission for the Exhibition of 1851 and a University Research Fellowship (URF\1\180088) from the Royal Society. Seismic data used in this study were retrieved from all data centers within the Federation for Digital Seismograph Networks data centers, principally the Incorporated Research Institutions for Seismology Data Management Center, the Southern California Earthquake Data Centre, the Northern California Earthquake Data Centre, and the Observatories and Research Facilities for European Seismology. Much of the data processing was done using the ObsPy package (Beyreuther et al., 2010). Several figures also used the Generic Mapping Tools software package (Wessel et al., 2013). I thank Andrew Walker for his assistance with the trials and tribulations of Python coding, Sebastian Rost for providing the code to calculate synthetic body waves to the required frequencies, and Christian Sippl for making his relocated microseismic catalogue available. I also thank the Associate Editor, one anonymous reviewer, and Manuel A. Florez for their comments on the manuscript.

References

Abe, K. (1974). Fault parameters determined by near- and far-field data: The Wakasa Bay earthquake of March 26, 1963. *Bulletin of the Seismological Society of America*, *64*, 1369–1382.

Baillard, C., Crawford, W., Ballu, V., Hibert, C., & Mangeney, A. (2014). An automatic kurtosis-based *P*- and *S*-phase picker designed for local seismic networks. *Bulletin of the Seismological Society of America*, *104*, 394–409. https://doi.org/10.1785/0120120347

Beyreuther, M., Barsch, R., Krischer, L., Megies, T., Behr, Y., & Wassermann, J. (2010). ObsPy: A Python toolbox for seismology. *Seismological Research Letters*, *81*, 530–533. https://doi.org/10.1785/gssrl.81.3.530

Bhattacharya, S., Ghose, A., Suresh, G., Baidya, P., & Saxena, R. (1997). Source parameters of Jabalpur earthquake of 22 May 1997. *Current Science*, *73*, 855–863.

Bondár, I., Myers, S. C., Engdahl, E. R., & Bergman, E. A. (2004). Epicentre accuracy based on seismic network criteria. *Geophysical Journal International*, *156*, 483–496. https://doi.org/10.1111/j.1365-246X.2004.02070

Bonner, J. L., Reiter, D. T., & Shumway, R. H. (2002). Application of a Cepstral *F* statistic for improved depth estimation. *Bulletin of the Seismological Society of America*, *92*, 1675–1693.

Craig, T. J., Copley, A., & Jackson, J. (2012). Thermal and tectonic consequences of India underthrusting Tibet. *Earth and Planetary Science Letters*, *353-354*, 231–239. https://doi.org/10.1016/j.epsl.2012.07.010

Craig, T. J., Copley, A., & Jackson, J. (2014). A reassessment of outer-rise seismicity and its implications for the mechanics of oceanic lithosphere. *Geophysical Journal International*, *197*, 63–89. https://doi.org/10.1093/gji/ggu013

Craig, T. J., & Heyburn, R. (2015). An enigmatic earthquake in the continental mantle lithosphere of stable North America. *Earth and Planetary Science Letters*, *425*, 12–23. https://doi.org/10.1016/j.epsl.2015.05.048

Craig, T. J., Jackson, J. A., Priestley, K., & McKenzie, D. (2011). Earthquake distribution patterns in Africa: Their relationship to variations in lithospheric and geological structure, and their rheological implications. *Geophysical Journal International*, *185*, 403–434. https://doi.org/10.1111/j.1365-246X.2011.04950.x

Crotwell, H. P., Owens, T., & Ritsema, J. (1999). The TauP Toolkit: Flexible seismic travel-time and ray-path utilities. *Seismological Research Letters*, *70*, 154–160.

Devlin, S., Isacks, B. L., Pritchard, M. E., Barnhart, W. D., & Lohman, R. B. (2012). Depths and focal mechanisms of crustal earthquakes in the central Andes determined from teleseismic waveform analysis and InSAR. *Tectonics*, *31*, TC2002. https://doi.org/10.1029/2011TC002914

Ekström, G., Nettles, M., & Dziewonski, A. (2012). The global CMT project 2004-2010: Centroid-moment tensors for 13,017 earthquakes. *Physics of the Earth and Planetary Interiors*, *200-201*, 1–9. https://doi.org/10/1016/j.pepi.2012.04.002

Engdahl, E. R., Jackson, J. A., Myers, S. C., Bergman, E. A., & Priestley, K. (2006). Relocation and assessment of seismicity in the Iran region. *Geophysical Journal International*, *167*, 761–778. https://doi.org/10.1111/j.l365-246X.2006.03127

Engdahl, E., van der Hilst, R., & Buland, R. (1998). Global teleseismic earthquake relocation with improved travel times and procedures for depth determination. *Bulletin of the Seismological Society of America*, *88*, 722–743.

Florez, M., & Prieto, G. (2017). Precise relative earthquake depth determination using array processing techniques. *Journal of Geophysical Research: Solid Earth*, *122*, 4559–4571. https://doi.org/10.1002/2017JB014132

Forsyth, D. W. (1982). Determination of focal depths of earthquakes associated with the bending of oceanic plates at trenches. *Physics of the Earth and Planetary Interiors*, *28*, 141–160.

Geller, R., & Ohminato, T. (1994). Computation of synthetic seismograms and their partial derivatives for heterogeneous media with arbitrary natural boundary conditions using the direct solution method. *Geophysical Journal International*, *116*, 421–446. https://doi.org/10.1111/j.1365-246X.1994.tb01807.x

Hayes, G. (2017). The finite, kinematic rupture properties of great-sized earthquakes since 1990. *Earth and Planetary Science Letters*, *468*, 94–100. https://doi.org/10.1016/j.epsl.2017.04.003

Hayes, G., Moore, G., Portner, D., Hearne, M., Flamme, H., Furtney, M., & Smocyzk, G. (2018). Slab2: A comprehensive subduction zone geometry. *Science*, *362*, 6410. https://doi.org/10.1126/science.aat4723

Heyburn, R., & Bowers, D. (2008). Earthquake depth estimation using the *F* Trace and Associated Probability. *Bulletin of the Seismological Society of America*, *98*, 18–35. https://doi.org/10.1785/0120070008

Huang, J., Niu, F., Gordon, R., & Cui, C. (2015). Accurate focal depth determination of oceanic earthquakes using water-column reverberation and some implications for the shrinking plate hypothesis. *Earth and Planetary Science Letters*, *432*, 133–141. https://doi.org/10.1016/j.epsl.2015.10.001

Huang, P. Y., Solomon, S., Bergman, E. A., & Nabelek, J. (1986). Focal depths and mechanisms of mid-atlantic ridge earthquakes from body waveform inversion. *Journal of Geophysical Research*, *91*, 579–598.

Husen, S., Kissling, E., Flueh, E., & Asch, G. (1999). Accurate hypocenter determination in the shallow part of the Nazca subduction zone in Northern Chile using a combined on/offshore network. *Geophysical Journal International*, *138*, 687–701.

Kanasewich, E. (1981). *Time Sequence Analysis in Geophysics*. Edmonton, Alberta: University of Alberta Press.

Kennett, B. L. N., Engdahl, E. R., & Buland, R. (1995). Constraints on seismic velocities in the Earth from travel times. *Geophysical Journal International*, *122*, 108–124.

Langston, C. (1976). A body wave inversion of the Koyna, India, earthquake of December 10, 1967, and some implications for body wave focal mechanisms. *Journal of Geophysical Research*, *81*, 2517–2529.

Letort, J., Guilbert, J., Cotton, F., Bondár, I., Cano, Y., & Vergoz, J. (2015). A new, improved and fully automatic method for teleseismic depth estimation of moderate earthquakes ($4.5 < M < 5.5$): Application to the Guerrero subduction zone (Mexico). *Geophysical Journal International*, *201*, 1834–1848. https://doi.org/10.1093/gji/ggv093

Letort, J., Vergoz, J., Guilbert, J., Cotton, F., Sebe, O., & Cano, Y. (2014). Moderate earthquake teleseismic depth estimations: New methods and use of the comprehensive nuclear-test-ban treaty organization network data. *Bulletin of the Seismological Society of America*, *104*, 593–607. https://doi.org/10.1785/0120130126

Maggi, A., Jackson, J. A., Priestley, K., & Baker, C. (2000). A re-assessment of focal depth distributions in southern Iran, the Tien Shan, and northern India: Do earthquakes really occur in the continental mantle? *Geophysical Journal International*, *143*, 629–661.

Murphy, J., & Barker, B. (2006). Improved focal-depth determination through automated identification of the seismic depth phases *pP* and *sP*. *Bulletin of the Seismological Society of America*, *96*, 1213–1229. https://doi.org/10.1785/0120050259

Purnachandra Rao, N., Tsukuda, T., Kosuga, M., Bhatia, S., & Suresh, G. (2002). Deep lower crustal earthquakes in central India: Inferences from analysis of regional broadband data of the 1997 May 21 Jabalpur earthquake. *Geophysical Journal International*, *148*, 132–138. https://doi.org/10.1046/j.0956-540x2001.01584.x

Ramesh, D., & Estabrook, C. (1998). Rupture histories of two stable continental region earthquakes in India. *Proceedings of the Indian Academy of Sciences*, *107*, 225–233.

Ross, Z., & Ben-Zion, Y. (2014). Automatic picking of direct *P*, *S* seismic phases and fault zone head waves. *Geophysical Journal International*, *199*, 368–381. https://doi.org/10.1093/gji/ggu267

Rost, S., & Thomas, C. (2002). Array seismology: Methods and applications. *Reviews of Geophysics*, *40*(3), 1008. https://doi.org/10.1029/2000RG0001002002

Saragiotis, C., Hadjileontiadis, L., & Panas, S. (2002). PAI-SK: A robust automatic seismic *P* phase arrival identification scheme. *IEEE Transactions on Geoscience and Remote Sensing*, *40*, 1395–1404. https://doi.org/10.1109/TGRS.2002.800438

Selby, N. (2011). Improved teleseismic signal detection at small-aperture arrays. *Bulletin of the Seismological Society of America*, *101*, 1563–1575. https://doi.org/10.1785/0120100253

Singh, S., Dattatrayam, R. S., Shapiro, N. M., Mandal, P., Pacheco, J. F., & Midha, R. K. (1999). Crustal and upper mantle structure of peninsular india and source parameters of the 21 May 1997, Jabalpur Earthquake ($M_w = 5.8$): Results from a new regional broadband network. *Bulletin of the Seismological Society of America*, *89*, 1631–1641.

Sippl, C., Schurr, B., Asch, G., & Kummerow, J. (2018). Seismicity structure of the northern Chile forearc from >100,000 double-difference relocated hypocenters. *Journal of Geophysical Research: Solid Earth*, *123*, 4063–4087. https://doi.org/10.1002/2017JB015384

Sloan, R. A., Jackson, J. A., McKenzie, D., & Priestley, K. (2011). Earthquake depth distribution in central Asia, and their relations with lithosphere thickness, shortening and extension. *Geophysical Journal International*, *185*, 1–29. https://doi.org/10.1111/j.1365-246X.2010.04882.x

Solomon, S., & Huang, P. (1987). Centroid depths and mechanisms of mid-ocean ridge earthquakes in the Indian Ocean, Gulf of Aden, and Red Sea. *Journal of Geophysical Research*, *92*, 1361–1382.

Wang, X., Wei, S., & Wu, W. (2017). Double-ramp on the Main Himalayan Thrust revealed by broadband waveform modeling of the 2015 Gorkha earthquake sequence. *Earth and Planetary Science Letters*, *473*, 83–93. https://doi.org/10.1016/j.epsl.2017.05.032

Wessel, P., Smith, W., Scharroo, R., Luis, J., & Wobbe, F. (2013). Generic mapping tools: Improved version released. *EOS Transactions*, *94*, 409–410.

Weston, J., Engdahl, E., Harris, J., Di Giacomo, D., & Stochak, D. (2018). ISC-EHB: Reconstruction of a robust earthquake data set. *Geophysical Journal International*, *214*, 474–484. https://doi.org/10.1093/gji/ggy155

Woodgold, C. (1999). Wide-Aperture beamforming of depth phases by timescale contraction. *Bulletin of the Seismological Society of America*, *89*, 165–177.

Yang, Z., & Chen, W.-P. (2010). Earthquakes along the East African Rift System: A multi-scale, system-wide perspective. *Journal of Geophysical Research*, *115*, B12309. https://doi.org/10.1029/2009JB006779